28 September 2012 | $10

Science

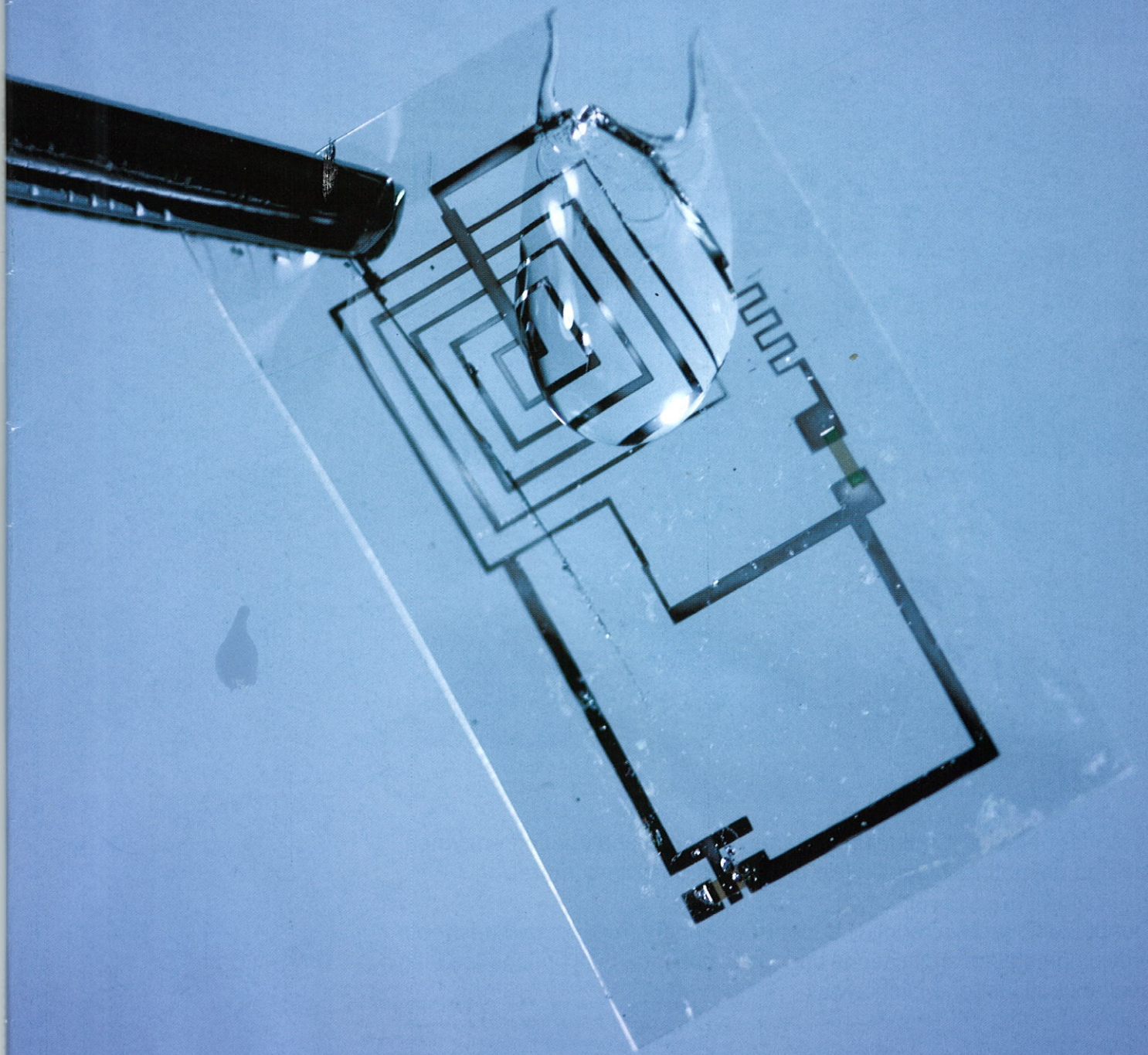

AAAS

A Physically Transient Form of Silicon Electronics

Suk-Won Hwang *et al.*

Science **337**, 1640 (2012);
DOI: 10.1126/science.1226325

Science (print ISSN 0036-8075; online ISSN 1095-9203) is published weekly, except the last week in December, by the American Association for the Advancement of Science, 1200 New York Avenue NW, Washington, DC 20005.

by a 3 to 10% perturbation in the local rotation rate in the outer few percent of the Sun (*16*).

Finally, the Sun's mean hexadecapole shape amplitude is small (–0.1 ± 0.4 milli–arc sec) but shows a hint of variability (*21*). This value is marginally correlated with the sunspot cycle with an amplitude of 2.1 ± 2 milli–arc sec. The hexadecapole shape is also sensitive to the internal solar differential rotation, but if due only to rotation, it would require large changes (on the order of 50%) in the outer parts of the Sun (*16*) that are not consistent with the constant helioseismic rotation (*20*) and the constant oblateness. In contrast, solar-cycle changes in near-surface flows or magnetic stresses localized near mid-latitudes could affect C_4 and not the oblateness.

References and Notes

1. R. H. Dicke, *Nature* **202**, 432 (1964).
2. H. A. Hill, R. T. Stebbins, *Astrophys. J.* **200**, 477 (1975).
3. R. H. Dicke, J. R. Kuhn, K. G. Libbrecht, *Astrophys. J.* **318**, 451 (1987).
4. A. Egidi *et al.*, *Sol. Phys.* **235**, 407 (2006).
5. J. Rösch, J. P. Rozelot, H. Deslandes, V. Desnoux, *Sol. Phys.* **165**, 1 (1996).
6. C. Damiani, J. P. Rozelot, S. Lefebvre, A. Kilcik, A. G. Kosovichev, *J. Atmos. Sol. Terr. Phys.* **73**, 241 (2011).
7. M. Emilio, R. Bush, J. R. Kuhn, P. Scherrer, *Astrophys. J.* **660**, L161 (2007).
8. M. D. Fivian, H. S. Hudson, R. P. Lin, H. J. Zahid, *Science* **322**, 560 (2008).
9. J. P. Rozelot, C. Damiani, *Eur. Phys. J. H* **36**, 407 (2011).
10. J. R. Kuhn, R. I. Bush, X. Scheick, P. Scherrer *Nature* **392**, 155 (1998).
11. We let $L(r,\theta)$ be the observed LDF function from a binned satellite image. From this, we used the circular average mean LDF represented by $\Gamma(r)$ to solve for a brightness function $\alpha(\theta)$ and the limb shape $\beta(\theta)$. The binned LDF function was then expressed as $L(r,\theta) = [\alpha(\theta) + 1]\Gamma[r - \beta(\theta)]$, where α and β represent the mean limb brightness change and position around the limb. We then linearized this equation and solved it as a least-squares problem to find α and β. We obtained the function $\Gamma(r)$ from the binned intensity of limb pixels, whereas we iterated the solution for $\beta(\theta)$ so that $\Gamma(r)$ was adjusted at each iteration by correcting the limb-pixel binning by shifting pixels by the local $\beta(\theta)$ from the previous iteration. This was done for each of the typically 13,000 images obtained during an SDO spacecraft roll. After two iterations, the solution was stable to better than 5%.
12. J. Schou *et al.*, *Sol. Phys.* **275**, 229 (2012).
13. Figure S1 shows that the analysis recovers the limb shape, independent of any limb brightness variations. Figure S2 shows that independent simultaneous HMI solar-limb shape and brightness measurements agree on all angular scales and that the limb position and brightness measurements are dominated by solar atmosphere inhomogeneity and its global asphericity.
14. R. J. Bray, R. E. Loughheed, *Sunspots* (Wiley, New York, 1965).
15. Figure S3 shows how the limb brightness and position are correlated and how the brightness measurements [α, see (*11*)] can be used to flag localized magnetic limb contamination of the limb shape. The shape analysis is broadly insensitive to the brightness threshold, with no significant change in the derived global oblateness, even with large changes in the assumed brightness threshold.
16. J. D. Armstrong, J. R. Kuhn, *Astrophys. J.* **525**, 533 (1999).
17. The χ^2statistic for these 5 degrees of freedom and a constant to describe the Fig. 4 C_2 data are both equal to 2.8. This indicates no statistical basis for a nonconstant C_2 at better than the 99.9% confidence level.
18. J. R. Kuhn, M. Emilio, R. Bush, *Science* **324**, 1143 (2009).
19. R. I. Bush, M. Emilio, J. R. Kuhn, *Astrophys. J.* **716**, 1381 (2010).
20. R. Howe, *Living Rev. Sol. Phys.* **6**, 1 (2009).
21. The χ^2 statistic for describing the hexadecapole amplitude as a constant was 9.4. This was marginally inconsistent (at 95% level) with a constant. Linear regression of the hexadecapole measurements against the sunspot number time series suggested a marginally significant hexadecapole solar-cycle variation with an amplitude of 2.1 ± 2 milli–arc sec.

Acknowledgments: The raw and astrometric data used for this analysis are available via the HMI public archives (http://jsoc.stanford.edu). The development of the HMI astrometry pipeline was supported by NASA and a grant to Stanford Univ. and the Univ. of Hawaii (NNX09AI90G). The HMI experiment aboard the SDO satellite was funded, in part, by a NASA contract to Stanford (NAS5-02139). J.R.K. was supported by a senior Humboldt prize while some of this work was done at the Kiepenheuer Institut fur Sonnenphysik. M.E. was partially supported by Instituto Nacional de Estudos do Espaço (CNPq), CNPq grant 303873/2010-8, and Coordenação de Aperfeiçoamento de Pessoal de Nivel Superior grant 0873/11-0. We thank H. Hudson for comments on this manuscript.

Supplementary Materials

www.sciencemag.org/cgi/content/full/science.1223231/DC1
Supplementary Text
Figs. S1 to S3
Table S1
References

11 April 2012; accepted 7 August 2012
Published online 16 August 2012;
10.1126/science.1223231

A Physically Transient Form of Silicon Electronics

Suk-Won Hwang,[1]* Hu Tao,[2]* Dae-Hyeong Kim,[3]* Huanyu Cheng,[4] Jun-Kyul Song,[5] Elliott Rill,[1] Mark A. Brenckle,[2] Bruce Panilaitis,[2] Sang Min Won,[6] Yun-Soung Kim,[1] Young Min Song,[1] Ki Jun Yu,[6] Abid Ameen,[1] Rui Li,[4,7] Yewang Su,[4] Miaomiao Yang,[2] David L. Kaplan,[2] Mitchell R. Zakin,[8] Marvin J. Slepian,[9] Yonggang Huang,[4] Fiorenzo G. Omenetto,[2,10]† John A. Rogers[1,5,6]†

A remarkable feature of modern silicon electronics is its ability to remain physically invariant, almost indefinitely for practical purposes. Although this characteristic is a hallmark of applications of integrated circuits that exist today, there might be opportunities for systems that offer the opposite behavior, such as implantable devices that function for medically useful time frames but then completely disappear via resorption by the body. We report a set of materials, manufacturing schemes, device components, and theoretical design tools for a silicon-based complementary metal oxide semiconductor (CMOS) technology that has this type of transient behavior, together with integrated sensors, actuators, power supply systems, and wireless control strategies. An implantable transient device that acts as a programmable nonantibiotic bacteriocide provides a system-level example.

An overarching goal in the development of nearly any new class of electronics is to achieve high-performance operation in physical forms that undergo negligible change with time. Active and passive materials, device and circuit layouts, and packaging strategies are each formulated individually and then configured collectively to accomplish this outcome. Here we present concepts and strategies for electronics that involve similar attention to engineering designs, but with the goal of achieving systems that physically disappear at prescribed times and at controlled rates. Applications that could exploit this transient behavior include implantable medical diagnostic and therapeutic devices that resorb in the body to avoid adverse long-term effects, fieldable environmental sensors that dissolve to eliminate the need for their retrieval, and portable consumer devices that decompose to minimize the costs and health risks associated with recycling and the management of hazardous waste streams. For these three examples, the desired time scales for transience range from days or weeks, to months, to years, respectively. The approaches reported here can address these and other application concepts with circuit components whose operational characteristics match those of nontransient counterparts formed in the usual way on silicon wafer substrates. When combined with transient sensors, actuators, power supplies, and wireless control systems, this technology provides levels of function that substantially exceed those available

[1]Department of Materials Science and Engineering, Beckman Institute for Advanced Science and Technology, and Frederick Seitz Materials Research Laboratory, University of Illinois at Urbana–Champaign, Urbana, IL 61801, USA. [2]Department of Biomedical Engineering, Tufts University, Medford, MA 02155, USA. [3]School of Chemical and Biological Engineering, Center for Nanoparticle Research of Institute for Basic Science, WCU Program of Chemical Convergence for Energy and Environment, Seoul National University, Seoul 151-741, Republic of Korea. [4]Department of Mechanical Engineering and Department of Civil and Environmental Engineering, Northwestern University, Evanston, IL 60208, USA. [5]Department of Chemistry, University of Illinois at Urbana–Champaign, Urbana, IL 61801, USA. [6]Department of Electrical and Computer Engineering, University of Illinois at Urbana–Champaign, Urbana, IL 61801, USA. [7]State Key Laboratory of Structural Analysis for Industrial Equipment, Department of Engineering Mechanics, Dalian University of Technology, Dalian 116024, China. [8]Nano Terra, Brighton, MA 02135, USA. [9]Department of Medicine and Department of BioMedical Engineering, Sarver Heart Center, University of Arizona, Tucson, AZ 85724, USA. [10]Department of Physics, Tufts University, Medford, MA 02155, USA.

*These authors contributed equally to this work.
†To whom correspondence should be addressed. E-mail: jrogers@uiuc.edu (J.A.R.); fiorenzo.omenetto@tufts.edu (F.G.O.)

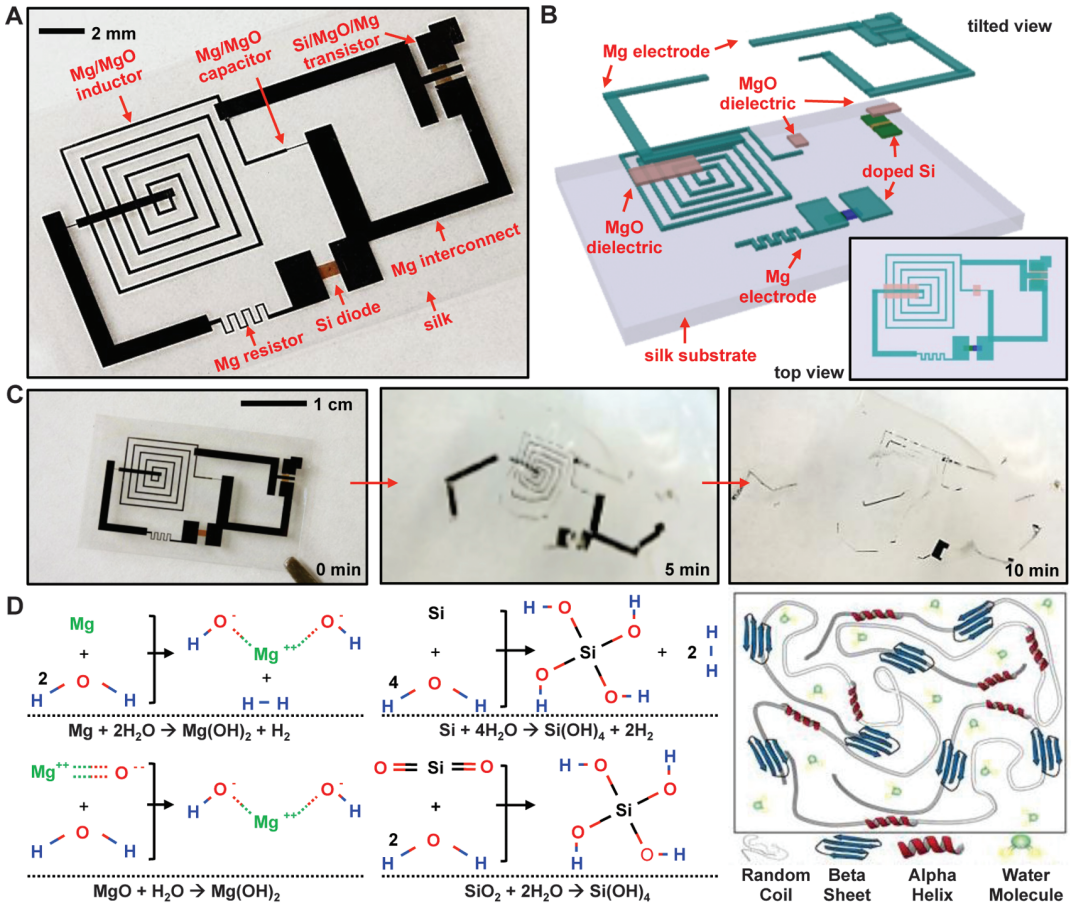

Fig. 1. Demonstration platform for transient electronics, with key materials, device structures, and reaction mechanisms. (**A**) Image of a device that includes transistors, diodes, inductors, capacitors, and resistors, with interconnects and interlayer dielectrics, all on a thin silk substrate. (**B**) Exploded-view schematic illustration, with a top view in the lower right inset. (**C**) Images showing the time sequence of dissolution in DI water. (**D**) Chemical reactions for each of the constituent materials with water.

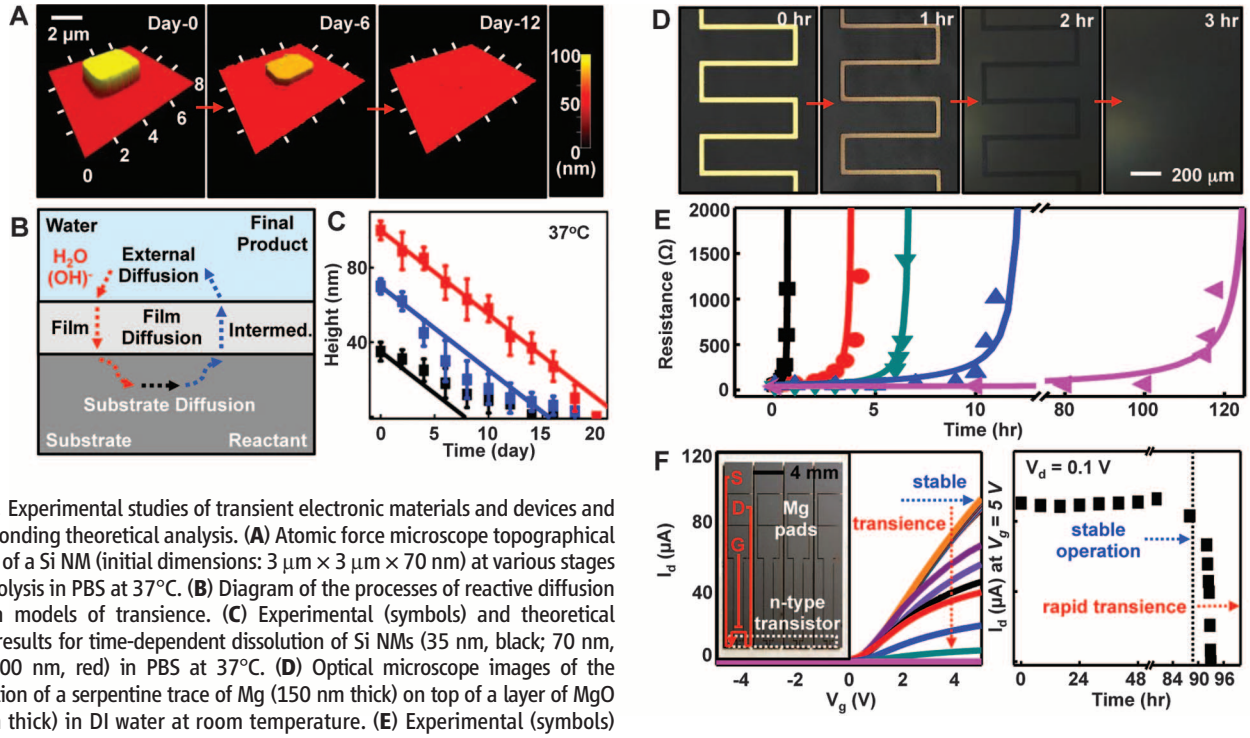

Fig. 2. Experimental studies of transient electronic materials and devices and corresponding theoretical analysis. (**A**) Atomic force microscope topographical images of a Si NM (initial dimensions: 3 μm × 3 μm × 70 nm) at various stages of hydrolysis in PBS at 37°C. (**B**) Diagram of the processes of reactive diffusion used in models of transience. (**C**) Experimental (symbols) and theoretical (lines) results for time-dependent dissolution of Si NMs (35 nm, black; 70 nm, blue; 100 nm, red) in PBS at 37°C. (**D**) Optical microscope images of the dissolution of a serpentine trace of Mg (150 nm thick) on top of a layer of MgO (10 nm thick) in DI water at room temperature. (**E**) Experimental (symbols) and theoretical (lines) results of dissolution kinetics of similar traces of Mg (300 nm thick) with different encapsulating layers: MgO (400 nm, red; 800 nm, blue) and silk (condition i, cyan; condition ii, purple). (**F**) Measurements of transience in operational characteristics of n-channel transistors encapsulated by MgO and crystallized silk (picture in the inset on the left) and then immersed in DI water. The results show the drain current (I_d) at V_d = 0.1 V as a function of V_g at various times (left) and at V_g = 5 V as a function of time (right).

with recently reported forms of organic electronics, in which certain constituent materials are water-soluble (*1*–*3*), or with simple nontransient transistors formed on bioresorbable substrates (*4*).

Figure 1, A and B, and fig. S1 provide images and schematic diagrams of a demonstration platform. All of the components, ranging from the inductors, capacitors, resistors, diodes, transistors, interconnects, and crossovers, to the substrate and encapsulation, disintegrate and dissolve when immersed in deionized (DI) water (Fig. 1C). This example uses magnesium (Mg) for the conductors, magnesium oxide (MgO) (silicon dioxide, SiO_2, is also possible) for the dielectrics, monocrystalline silicon (Si) nanomembranes (NMs) for the semiconductors, and silk (which is water-soluble and enzymatically degradable) (*4*, *5*) for the substrate and packaging material. The fabrication of systems such as this one involves a combination of transfer printing (Si NMs) (*6*), physical vapor deposition through fine-line stencil masks (Mg, MgO, and SiO_2), and solution-casting (silk). More details on sample preparation can be found in (*6*). As adhesion promoters for Mg, we used MgO in certain cases and ultrathin layers of Ti in others. Device yields without the Ti are 70 to ~80% with evaporated Mg and >90% with sputtered Mg.

The chemical reactions responsible for the dissolution of each material appear in Fig. 1D. The Si NMs and layers of SiO_2 are particularly important because of their essential roles in high-performance transistors, diodes, photodetectors, solar cells, temperature sensors, strain gauges, and other semiconductor devices. The NM geometry is critical because it enables high-performance devices and planar architectures, minimizes the amount of material that must be consumed during the transient step, and provides mechanics and processing options that are favorable for heterogeneous integration onto substrates such as silk (*4*), as well as elastomers that can provide modulus-matched interfaces with the body (*7*). A typical transistor described here requires less than ~1 μg of Si, which can be dissolved in as little as 30 μl of biofluid (*8*).

Figure 2A presents atomic force micrographs of a Si NM (3 × 3 μm) with a thickness of 70 nm, collected at different stages of dissolution in phosphate-buffered saline (PBS; pH of 7.4) at 37°C, to simulate transience by bioresorption (see figs. S2 and S3A for additional data). The dissolution involves hydrolysis to form $Si(OH)_4$ (*9*), according to $Si + 4\ H_2O \leftrightarrow Si(OH)_4 + 2\ H_2$, where SiO_2 can sometimes be involved as an intermediate (*10*). The simplest model of the kinetics, which depends strongly on pH, considers a constant reaction rate at the water/Si NM interface (*11*). The results capture experimental observations at both body temperature (37°C) (Fig. 2C) and room temperature (25°C) (fig. S3A) for a dissolution rate of 4.5 nm/day and 2 nm/day, respectively, consistent with Arrhenius scaling (*12*).

Mechanisms involving diffusion into the materials can be important for Mg and MgO deposited by electron-beam evaporation and SiO_2 formed by chemical vapor deposition, or as an intermediate in the hydrolysis of Si. In such cases, the kinetics can be described analytically using models of reactive diffusion (Fig. 2B) (*6*). The results quantitatively account for related behaviors in other materials for transient electronics, including those in Fig. 1 (*6*). Figure 2D presents a meander trace of Mg (150 nm) on a thin film of MgO (10 nm; adhesion promoter), in which the measured changes in resistance correlate well with those expected based on computed changes in thickness (Fig. 2E and fig. S4, A and B) (*6*). (Other examples appear in fig. S5.) This result connects a key electrical property to models of reactive diffusion, thereby suggesting the capacity to use such analytics in conjunction with established circuit simulators as a comprehensive design approach.

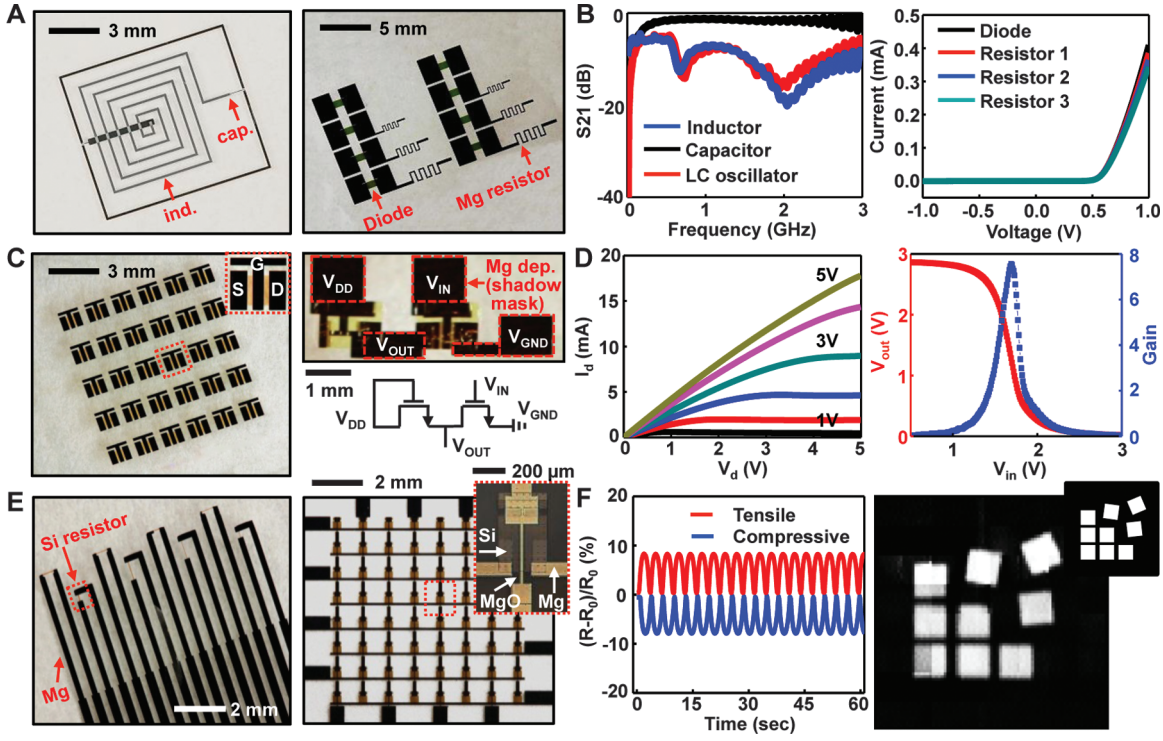

Fig. 3. Images and electrical properties of transient electronic components, circuits, and sensors, including simple integrated circuits and sensor arrays. (**A**) Image of an LC (inductor-capacitor) oscillator fabricated with Mg electrodes and MgO dielectric layers (left) and an array of Si NM diodes with serpentine Mg resistors (right). (**B**) Measurements of the S21 scattering parameter of an inductor (blue), capacitor (black), and LC oscillator (red) at frequencies up to 3 GHz (left). Current-voltage (*I-V*) characteristics of diodes connected to three different Mg resistors (right) are shown. (**C**) Images of an array of p-channel (left) MOSFETs and a logic gate (inverter; right) composed of n-channel MOSFETs. The MOSFETs use Mg source (S), drain (D), and gate (G) electrodes; MgO gate dielectrics; and Si NM semiconductors. The inverter uses Mg for interconnects and Au for source, drain, and gate electrodes, in a circuit configuration shown in the diagram. (**D**) *I-V* characteristics of a representative n-channel MOSFET [left, channel length (L_{ch}) and width (*W*) are 20 μm and 900 μm, respectively]. Transfer characteristic for the inverter (right, L_{ch} and *W* are 20 μm and 700 μm for the input transistor and 500 μm and 40 μm for the load transistor, respectively). The voltage gain is ~8. (**E**) Image of strain sensors based on Si NM resistors (left) and an addressable array of Si NM photodetectors with blocking diodes. In both cases, Mg serves as contact and interconnection electrodes and MgO as the dielectric. (**F**) Fractional change in resistance of a representative strain gauge as a function of time during cyclic loading (left). *R*, bent; R_0, flat. Bending induces tensile (red) and compressive (blue) strains uniaxially up to ~0.2%. Right, image of a logo collected with the photodetector array. The inset shows the logo design.

The transience times for NM-based electronic components can be extended, in controlled amounts, by adding transient encapsulating layers and packaging materials; they can be reduced by decreasing the critical dimensions or by physically structuring the materials in a way that accelerates dissolution by disintegration (fig. S6). Figure 2E and fig. S4 show results of measured transience in a serpentine resistor of Mg, encapsulated with different thicknesses of MgO and with combinations of MgO and overcoats of silk. Corresponding modeling results are also shown in (*6*). Silk is attractive for this purpose because its solubility in water can be programmed, over several orders of magnitude, through the control of crystallinity (*5*, *13*). Other biodegradable polymers can also be used, as shown in fig. S7.

Studies of transience at the device level are also important. Figure 2F shows examples of metal oxide semiconductor field-effect transistors (MOSFETs) formed using Si NMs, SiO_2 gate dielectrics, and Mg electrodes, with encapsulating layers of MgO and crystallized silk. The devices show two-stage kinetics in their functional transience. Immersion in DI water for up to ~90 hours causes negligible change in key device characteristics. Functional degradation then occurs in a relatively narrow time interval after this period of stable operation. The encapsulation defines the first time scale; the Mg electrodes define the second. The results demonstrate that the transience time can be engineered in a way that is decoupled from system- or device-level function.

These materials, fabrication techniques, and modeling tools can yield components for almost any type of transient electronic system, in CMOS designs. Figure 3 presents several examples, including additional details on MOSFETs similar to those in Fig. 2F, where both n- and p-channel operation is possible. The resulting electrical properties for an n-channel device include saturation and linear regime mobilities of 560 $cm^2/V{\cdot}s$ and 660 $cm^2/V{\cdot}s$, respectively, on/off ratios of $>10^5$, subthreshold slopes of 160 mV/dec [at drain voltage (V_d) = 0.1 V] and width-normalized current outputs of 0.34 mA/mm [at gate voltage (V_g) = 5 V]. These characteristics, as well as those of similar p-channel devices, compare favorably to the performance of counterparts formed on Si-on-insulator (SOI) wafers (*14*). [For the range of channel lengths investigated, contact resistances do not limit performance (fig. S8).] In all cases, the transience times of different elements in an integrated system can be controlled by use of varied thicknesses and/or stack compositions, or even via combination with nontransient materials. This last possibility is shown in a logic gate (inverter) in the righthand panels of Fig. 3, C and D, where a nontransient metal (Au) serves as source, drain, and gate electrodes for two transistors joined by transient Mg interconnects.

Many other classes of semiconductor devices and passive components are possible, with examples in Fig. 3 and figs. S9 and S10. The resistors and diodes can serve as temperature sensors; the latter can also be used in photodetectors and solar cells, as shown in Fig. 3 and fig. S10. The Si NM diode and Mg resistive temperature sensors show sensitivities of –2.23 mV/°C (change in

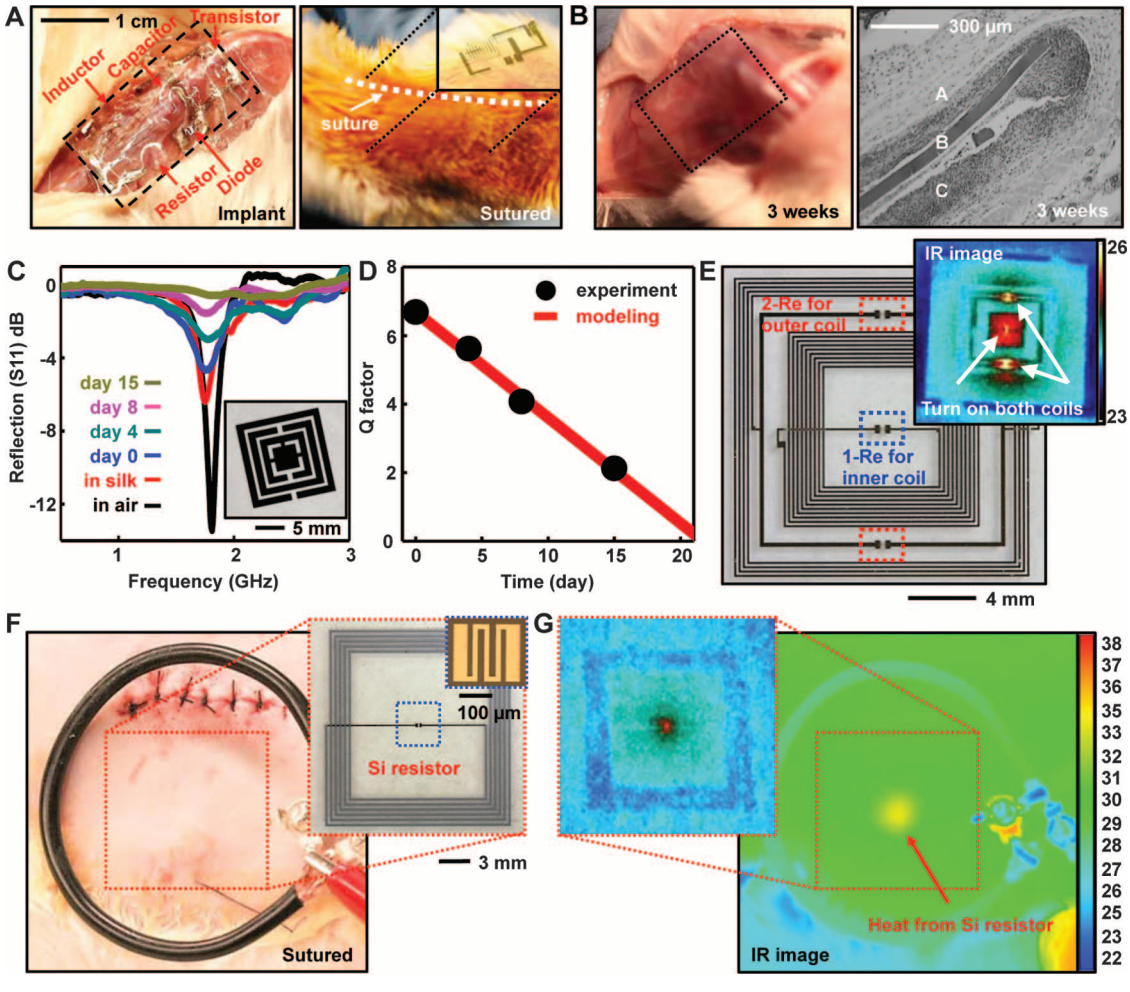

Fig. 4. In vivo evaluations and example of a transient bioresorbable device for thermal therapy. (**A**) Images of an implanted (left) and sutured (right) demonstration platform for transient electronics located in the subdermal dorsal region of a BALB/c mouse. (**B**) Implant site after 3 weeks (left). (Right) Histological section of tissue at the implant site, excised after 3 weeks, showing a partially resorbed region of the silk film. (A, subcutaneous tissue; B, silk film; C, muscle layer). (**C**) Resonant responses of an implanted transient rf metamaterial structure before and after placement in a silk package, immediately after implantation and at several time intervals thereafter. (**D**) Measured and calculated *Q* factor for the metamaterial. The results indicate transience dominated by the diffusion of biofluids through the silk package. (**E**) Transient wireless device for thermal therapy, consisting of two resistors (red outline) connected to a first wireless coil (70 MHz; outer coil) and a second resistor (blue outline) connected to a second, independently addressable, wireless coil (140 MHz; inner coil). The inset shows a thermal image of this device coupled with a primary coil operating at two frequencies, to drive both the inner and outer coils simultaneously. (**F**) Primary coil next to a sutured implant site for a transient thermal therapy device. The inset shows an image of a device. (**G**) Thermal image collected while wirelessly powering the device through the skin; the results show a hot spot (5°C above background) at the expected location, with a magnified view in the inset.

voltage for a given current output) and 0.23%/°C (percentage change in resistance), both of which are consistent with the behavior of conventional, nontransient devices (*15*). Ultrathin Si solar cells (~3 μm thick) provide fill factors of 66% and overall power conversion efficiencies of ~3%, even without light-trapping structures, backside reflectors, or antireflection coatings. Doped Si NMs can serve as strain gauges (Fig. 3E, left), with gauge factors of nearly ~40 (Fig. 3F, left, and fig. S10B), which are comparable to those of state-of-the art devices (*16*). As an example of interconnected components, we built a transient digital imaging system, consisting of collections of Si NM photodiodes with blocking diodes for passive matrix addressing (Fig. 3E, right), capable of capturing pictures when operated in a scanned mode (Fig. 3F, right, and fig. S10D). (See more details on device dimensions in fig. S11.) The yield here is >90% [i.e., 58 out of 64 pixels were fully functional (fig. S12)]. One possibility for power supply involves Si solar cells such as those shown in fig. S10A. Another uses inductors and capacitors like those in Figs. 1A and 3A and fig. S9 as wireless antennas for near-field mutual inductance coupling to separately powered, external primary coils. This option is interesting for implantable devices (*4*), made possible by the biocompatibility of the constituent materials (Fig. 1), as established in unrelated contexts (*6*).

To demonstrate opportunities, we conducted a series of in vivo and in vitro experiments. Various representative transient devices were fabricated, sealed in silk packages, sterilized with ethylene oxide, and then implanted in the subdermal region of BALB/c mice in accordance with Institutional Animal Care and Use Committee protocols. Figure 4A shows the case of the platform in Fig. 1. Examination after 3 weeks (Fig. 4B, left) revealed only faint residues, with evidence of slow reintegration into the subdermal layers, along with apparent revascularization. The histological section in Fig. 4B (right) shows the subdermal layer (A), the silk film (B), and the muscle layer (C) and reveals no significant inflammatory reactions. Additional analysis appears in fig. S13.

Inductive coils of Mg combined with resistive microheaters of doped Si NMs, integrated on silk substrates and housed in silk packages, can provide transient thermal therapy to control surgical site infections (*17*, *18*) as a nonantibiotic, programmable bacteriocidal appliqué that disappears as the patient moves beyond the period of greatest risk. In vitro tests demonstrate the efficacy of this approach (*6*). Figure 4, C and D, present a metamaterial rf antenna, as a generalized component for such a device, capable of continuous wireless monitoring after implantation. The data indicate transient behavior associated with the slow diffusion of biofluids through the edges of the silk package, with a measured quality (Q) factor that has time dependence consistent with theoretical models (*6*). Figure 4E shows an image of a functional device formed on glass that includes two coils with different resonance frequencies (~70 and ~140 MHz) and three separate heaters. Wirelessly operating either or both of these coils with appropriate frequencies and power levels applied to a separate primary coil enables full control of the system, as illustrated in the thermal image in the inset. (See figs. S14 to S16 for other examples.) To illustrate in vivo functionality, a fully transient version of this device was implanted under the skin of a Sprague-Dawley rat (Fig. 4F). Inductive coupling through the skin generates a localized temperature increase of ΔT ~5°C (Fig. 4G), coincident with the position of the heater. The functional transience has a time scale of 15 days, chosen via the crystallinity of the silk, to coincide with the most critical period, which is the first few days after an operation, to sterilize and maintain asepsis at the wound site. After this time, the device disappears, leaving only remnants of silk, which resorb on longer time scales, to eliminate the long-term burden associated with additional exogenous implant material.

Concepts reported here establish a baseline of materials, modeling approaches, manufacturing schemes, and device designs for transient electronic systems, sensors, actuators, and power supplies. The Si NMs are critically important elements, because their use enables sophisticated semiconductor components with both active and passive functionality. For the dielectrics and conductors, additional possibilities range from collagen to poly(lactic-co-glycolic acid) and from iron to zinc, respectively. Alternative modes of transience include absorption, corrosion, and depolymerization. The rates for these processes could, conceivably, be adjustable in real time and/or sensitive to the properties of the surrounding environment, determined by chemical or biological events, or changes in temperature, pressure, or light. Combining such possibilities in transience with ideas in soft, tissue-like electronics will further expand opportunities for applications in biomedical devices (*7*).

References and Notes

1. C. J. Bettinger, Z. Bao, *Adv. Mater.* **22**, 651 (2010).
2. M. Irimia-Vladu *et al.*, *Adv. Funct. Mater.* **20**, 4069 (2010).
3. C. Legnani *et al.*, *Thin Solid Films* **517**, 1016 (2008).
4. D.-H. Kim *et al.*, *Nat. Mater.* **9**, 511 (2010).
5. Y. Wang *et al.*, *Biomaterials* **29**, 3415 (2008).
6. Information on materials and methods is available in the supplementary materials on *Science* Online.
7. D.-H. Kim *et al.*, *Science* **333**, 838 (2011).
8. R. K. Iler, *J. Colloid Interface Sci.* **43**, 399 (1973).
9. J. D. Rimstidt, H. L. Barnes, *Geochim. Cosmochim. Acta* **44**, 1683 (1980).
10. M. Morita, T. Ohmi, E. Hasegawa, M. Kawakami, M. Ohwada, *J. Appl. Phys.* **68**, 1272 (1990).
11. H. Seidel, L. Csepregi, A. Heuberger, H. Baumgartel, *J. Electrochem. Soc.* **137**, 3612 (1990).
12. R. D. Levine, *Molecular Reaction Dynamics* (Cambridge Univ. Press, Cambridge, 2005).
13. X. Hu *et al.*, *Biomacromolecules* **12**, 1686 (2011).
14. H.-J. Chung *et al.*, *Adv. Funct. Mater.* **21**, 3029 (2011).
15. S. Santra, P. K. Guha, S. Z. Ali, I. Haneef, F. Udrea, *IEEE Sens. J.* **10**, 997 (2010).
16. S. M. Won *et al.*, *IEEE Trans. Electron Devices* **58**, 4074 (2011).
17. *Am. J. Infect. Control* **24**, 380 (1996).
18. D. J. Anderson *et al.*, *PLoS ONE* **4**, 1 (2009); http://dx.doi.org/10.1371/journal.pone.0008305.

Acknowledgments: The work on materials, integration schemes, manufacturing approaches, and design strategies was supported by the Defense Advanced Research Projects Agency. The theoretical analysis and associated experiments were supported by an NSF INSPIRE grant. The techniques for creating and manipulating Si nanomembranes were developed in work supported by an Air Force Office of Scientific Research Multi University Research Initiative program. The animal studies were funded by the National Institutes of Health (grant EB002520). The facilities for characterization and analysis were provided by the Material Research Laboratory and Center for Microanalysis of Materials at the University of Illinois at Urbana–Champaign, both of which are supported by the U.S. Department of Energy.

Supplementary Materials

www.sciencemag.org/cgi/content/full/337/6102/1640/DC1
Materials and Methods
Figs. S1 to S22
References (*19*–*32*)

19 June 2012; accepted 29 August 2012
10.1126/science.1226325

Gold-Catalyzed Direct Arylation

Liam T. Ball, Guy C. Lloyd-Jones,* Christopher A. Russell*

Biaryls (two directly connected aromatic rings, Ar^1-Ar^2) are common motifs in pharmaceuticals, agrochemicals, and organic materials. Current methods for establishing the Ar^1-Ar^2 bond are dominated by the cross-coupling of aryl halides (Ar^1-X) with aryl metallics (Ar^2-M). We report that, in the presence of 1 to 2 mole percent of a gold catalyst and a mild oxidant, a wide range of arenes (Ar^1-H) undergo site-selective arylation by arylsilanes (Ar^2-$SiMe_3$) to generate biaryls (Ar^1-Ar^2), with little or no homocoupling (Ar^1-Ar^1/Ar^2-Ar^2). Catalysis proceeds at room temperature and tolerates a broad range of functional groups, including those incompatible with cross-coupling. These features expedite biaryl preparation, as demonstrated by synthesis of the nonsteroidal anti-inflammatory diflunisal.

The biaryl moiety (two directly connected aromatic rings, Ar^1-Ar^2) is a common functionality in pharmaceuticals [such as Lipitor, Crestor, and Diovan, three of the most widely prescribed drugs in 2010 (*1*)]; in agrochemicals; and in many modern organic materials, including liquid crystal displays, light-emitting diodes, and conducting polymers. The